Design study of Beam Loss Monitoring system for the Rare Isotope Science Project in Korea

View the article online for updates and enhancements.

IOP ebooks™

Bringing you innovative digital publishing with leading voices to create your essential collection of books in STEM research.

Start exploring the collection - download the first chapter of every title for free.

Design study of Beam Loss Monitoring system for the Rare Isotope Science Project in Korea

Y.L. Cheon,[a] C.K. Sung,[a] K.J. Moon,[a] D.H. Kwak,[a] Y. Chung,[b] G.D. Kim,[b] H.J. Woo[b] and M. Chung[a,1]

[a]*Department of Physics, Ulsan National Institute of Science and Technology,*
Ulsan 44919, Korea

[b]*Rare Isotope Science Project, Institute for Basic Science,*
Daejeon 34047, Korea

E-mail: mchung@unist.ac.kr

ABSTRACT: A new heavy ion accelerator facility called RAON is being constructed in Daejeon, Korea to produce rare isotope beams of various energies for the Rare Isotope Science Project (RISP). This facility is designed to use both the In-flight Fragmentation (IF) and Isotope Separation On-Line (ISOL) systems to provide a wide range of rare isotope beams to be utilized in many fundamental physics experiments and in various applications. The RAON can use both stable heavy ion beams and rare isotope beams with energies up to a few hundreds of MeV/u with 400 kW of beam power. One of the greatest challenges in operating such a high beam power facility (~ 400 kW) is to accurately monitor the beam loss and trigger the Machine Protection System (MPS) reasonably quickly. In this paper, we report the conceptual design of the RAON beam loss monitoring system. Monte Carlo simulations using the MCNPX code were performed to understand beam loss-induced neutron and gamma radiation. The types of detectors were determined based on radiation simulations while considering the sensitivies of the detectors and response time requirements.

---

[1]Corresponding author.

Contents

1 Introduction

A new heavy ion accelerator facility called RAON is being constructed in Daejeon, Korea for the Rare Isotope Science Project (RISP) [1]. There are two rare isotope production systems at ROAN: the Isotope Separation On-Line (ISOL) and In-flight Fragmentation (IF) systems [2–4]. While the ISOL system uses light ion beams (e.g., 70 MeV protons) with a high Z nuclear target, the IF system uses heavy ion beams (e.g., 200 MeV/u uranium ions) with a low Z nuclear target to produce Rare Isotope Beams (RIBs). Each end of the ISOL and IF systems is connected to various experimental systems, such as the Korea Broad acceptance Recoil Spectrometer and Apparatus (KOBRA) and Large Acceptance Multi-Purpose Spectrometer (LAMPS) [2, 4, 5]. The RAON is expected to play an important role in nuclear physics research by taking advantage of high intensity RIBs and high performance experimental systems [2, 4, 6].

Figure 1 shows the overall layout of the RAON accelerator facility [2]. Both heavy ion beams ranging from protons to uranium and RIBs can be generated and delivered through the superconducting linear accelerator (linac) sections. Low energy stable ions or RIBs ranging from
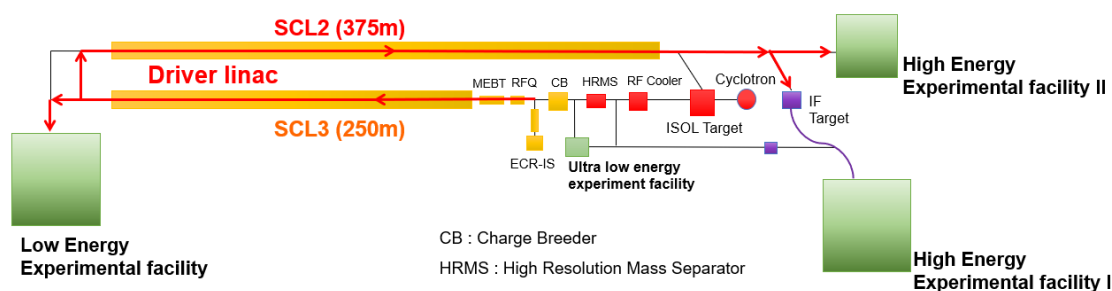
Figure 1. Layout of the RAON accelerator facility. Low energy stable ions and rare isotope beams are accelerated by the first superconducting linac (SCL3), and are further accelerated by the main driver linac (SCL2) up to 400 kW beam power.

a few to 18.5 MeV/u can be accelerated by the first superconducting linac (SCL3). Beams can be further accelerated through the main driver linac (SCL2), reaching up to a few hundreds of MeV/u with 400 kW beam power [3].
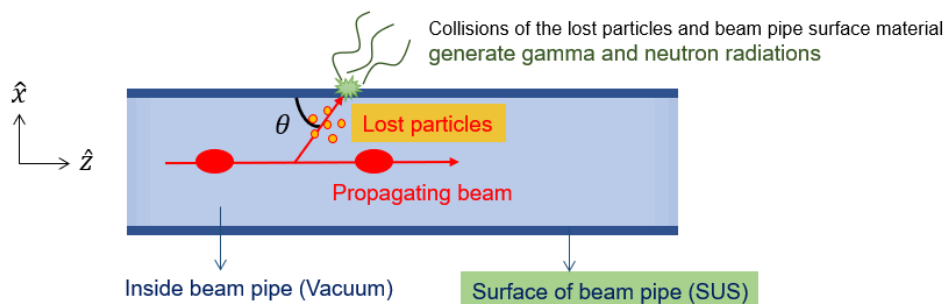

Figure 2. An illustration of beam loss during transport. Particles lost from the beam collide with the inner surface of the beam pipe, generating many secondary particles, gamma and neutron radiation, and causing damage to the beam line components.

While the beam is being transported through the beam pipe, some lost particles can deviate from their stable trajectories and generate unwanted radiation. There are two kinds of beam loss generation mechanisms: fast loss and slow loss. Fast losses are primarily caused by failure of accelerator components, thus they are unexpected and occur instantaneously. By contrast, slow losses primarily arise because of intrinsic beam transport characteristics, such as formation of the beam halo from nonlinear space charge effects [7–9], which are rather expected and occur slowly (these typically accumulate over 100 ms). The lost particles can collide with and be injected into the surface of the beam pipe, which causes serious damage to beam line components (see figure 2). Therefore, one of the greatest challenges in operating such a high beam power facility (~ 400 kW) is to accurately monitor beam loss and quickly trigger the machine protection system (MPS) [10, 11]. The Beam Loss Monitor (BLM) is one of the key elements of the MPS. It is used to protect beam line components from fast or slow losses, minimize activation of maintenance components,

and provide information for beam tuning and optimization. A BLM primarily detects gamma and neutron radiation which are generated through interactions between lost beam particles and atoms in the beam line components (see figure 2). To select and design the most appropriate BLM systems, many accelerator projects have relied on detailed numerical calculations of beam loss-induced radiation using different simulation tools, such as GEANT4 [12], MARS [13], FLUKA [14], and MCNPX [15]. In this work, we used the MCNPX simulation tool to predict and understand beam loss-induced radiation. This step is helpful for designing proper beam loss detectors.

2 Machine Protection System (MPS) requirements

2.1 Yield time

It is known that the yield stress of the beam line components (e.g., copper, stainless steel, or niobium) indeed determines the maximum allowable beam injection time (T_{max}) [11, 16–18]:

$$T_{max} \approx \frac{4\pi}{\sqrt{3}} \frac{\sigma_x \sigma_y}{I} \frac{\rho C_\nu}{\alpha E} \sigma_m \frac{1}{R_{avg}}, \tag{2.1a}$$

$$\frac{1}{R_{avg}} = \frac{1}{T} \int_0^T \frac{dT}{dT/dx} = \frac{R}{T}. \tag{2.1b}$$

In the above equations, σ_x (σ_y) is the RMS beam radius in the $x(y)$-direction, I is the peak beam current (particles per second), ρ is the mass density of the target material, C_ν is the specific heat, α is the coefficient of linear expansion, E is Young's modulus, σ_m is the material's yield strength, and R_{avg} is the average stopping power of the Bragg curve, which is estimated from the SRIM code [19]. The average stopping power can be calculated using eq. (2.1b), where R is the projected range of the beam into the material, and T is the incident beam energy. For a fixed incident beam energy, the projected range (R) is the total distance along the incident direction, which is constant regardless of the grazing angle of the beam. In addition, the RMS beam radius projected on the line of the beam pipe surface depends on the incident grazing angle. Figure 3 shows the injected beam sizes and ranges into the pipe material for different grazing angles θ. Unlike the projected range, the projected beam size increases by $1/\sin\theta$ as the grazing angle decreases, which means the maximum allowable time depends on θ, according to eq. (2.1a).

The maximum allowable injection time indeed determines the response time of the MPS. Because the stopping power of heavy ion beams is approximately a factor 10 larger than that of proton or electron beams, an MPS with a fast response is even more important in heavy ion machines. Figure 4 shows graphs of T_{max} for the cases of uranium and oxygen beams injected into stainless steel (SS) along the RISP linac (see figure 1). Equations (2.1) were used for these calculations, where it was assumed that all beam particles would be shifted and deviated from the ideal trajectories toward the inner surface of the beam pipe. We note that only the fast beam loss cases are considered here. The deformation time of SS by the oxygen beam grows more rapidly than that by uranium beam as the energy of incident beam increases. The energy of the uranium beam corresponding to the lowest value of T_{max} is higher than that of the oxygen beam. This is because the maximum value of R_{avg} corresponds to a higher incident energy in the case of uranium. For incident (grazing) angles larger than 60 degrees, beam line components may be damaged in
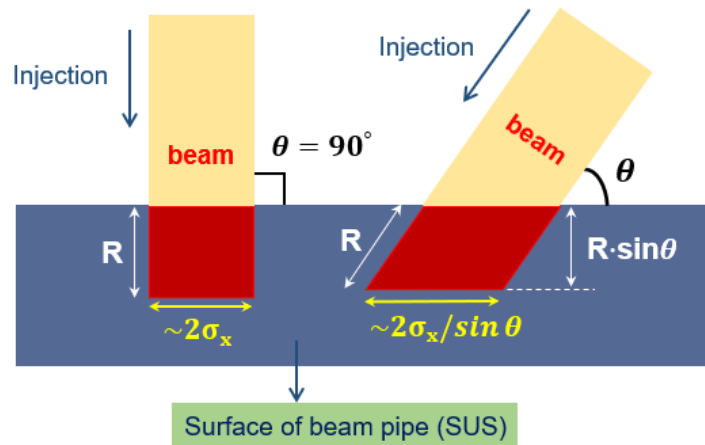
Figure 3. Beam injection mechanism with grazing angle, where R is the projected range of the beam into the material. (left) The worst case scenario in which the grazing angle is 90 degrees. This may occur only when beam hits the gate valve or bellows. (right) In most cases, the grazing angle would be small enough that the projected beam size increases by $1/\sin\theta$.

less than $20\,\mu s$, which is beyond the capability of the RISP MPS. A 90 degree angle is the worst case scenario and results in maximum damage to the components. Nevertheless, such a case may occur, for example only when objects (e.g., the gate valve) are in the beam line or the beam hits the bellows. In most cases, it is expected that the incident angle is small enough ($< 15°$) that a response time of $\sim 35\,\mu s$ would be reasonable to protect beam line components from catastrophic beam loss situations.

2.2 Melting time

We also simulated the melting time of beam line components after lost beam particles are injected into these components. The ANSYS simulation tool with transient thermal module was used to analyze the thermal behavior of Nb and SS, under the assumption that uranium beam has 1 mm RMS radius, Gaussian profile, and 90 degree grazing angle (i.e., the fast loss case). The energy of the incident uranium beam was set to $18.9\,\text{MeV/u}$ based on the $T_{\max}$ result in figure 4, which corresponds to the lowest allowable time for yield.

Figure 5 shows the temperature rise of SS and Nb as a function of the uranium beam injection time. Temperature rise over a short time period is primarily determined by the beam deposited power density and the specific heat of the material. The required time to reach the melting points of the two materials (SUS304: 1673–1723°C, Nb: 2750°C) are $\sim 46\,\mu s$ and $\sim 69\,\mu s$, respectively, which are longer than the overall MPS time requirement of $\sim 35\,\mu s$ estimated in section 2.1.

2.3 MPS response time

According to the results of sections 2.1 and 2.2, we note that the MPS in RAON must be executed within $35\,\mu s$. The target MPS response time of $35\,\mu s$ can be divided into the time required to detect an abnormal beam signal and assess whether the beam loss is abnormal (within $15\,\mu s$), the response
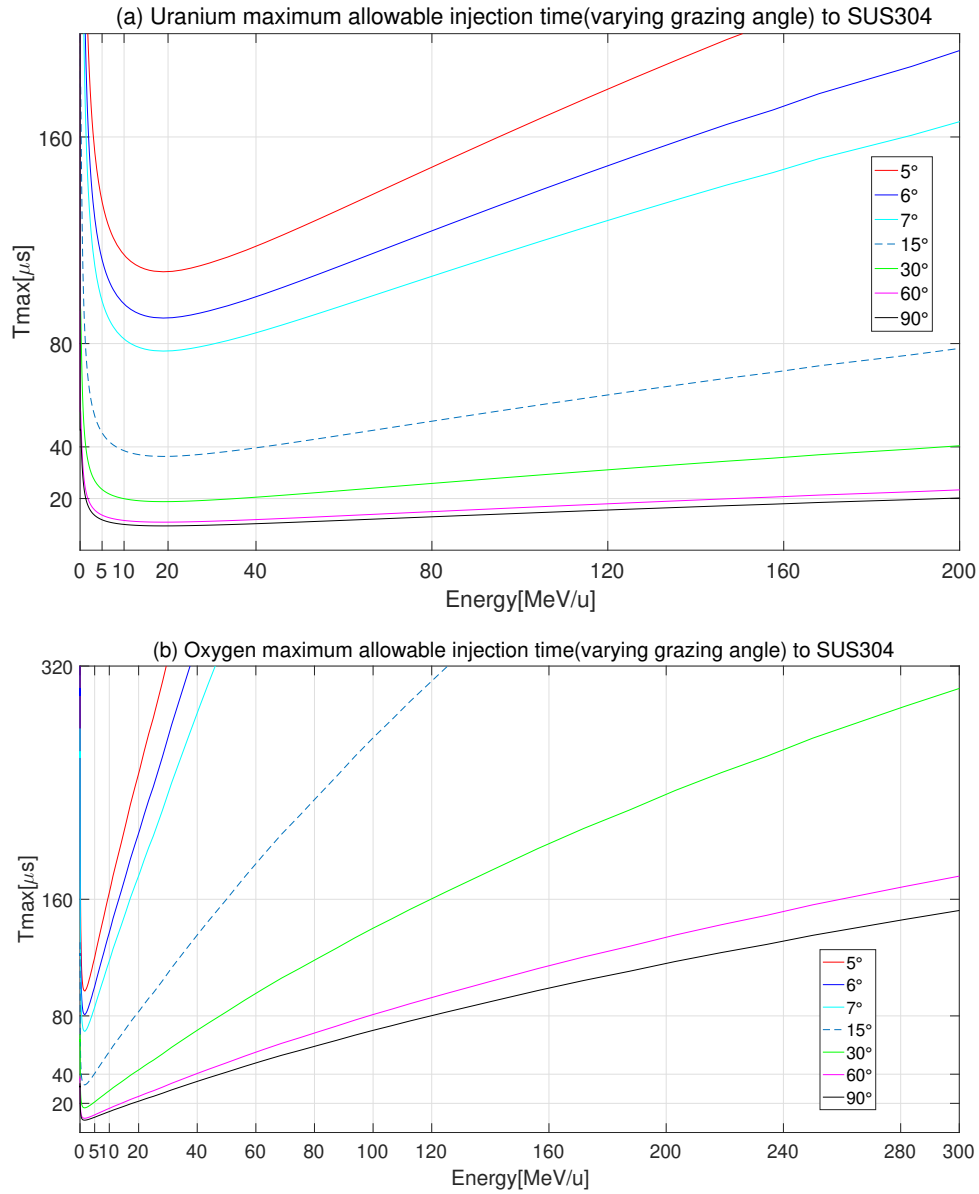
Figure 4. The maximum allowable beam injection time (T_{max}) in the fast loss case. T_{max} depends on the incidence (grazing) angle. (a) Uranium beam injection time on SS. (b) Oxygen beam injection time on SS.

time to respond to abnormal beam signals (within $10\,\mu s$), and the latent beam transmission time in the beam tunnel during the response time (within $10\,\mu s$).

For all processes to complete within $35\,\mu s$, signal must transmit between the BLM systems and control room through cables within a few μs. Therefore, we calculated the transfer time according to the length of the cable. An LMR-400 cable model is considered, in which the velocity of signal propagation is 85% of the speed of light. Figure 6 shows a graph of the signal transfer time as a function of cable length. Signals can be transmitted within several μs over a cable that is a few hundred meters long.
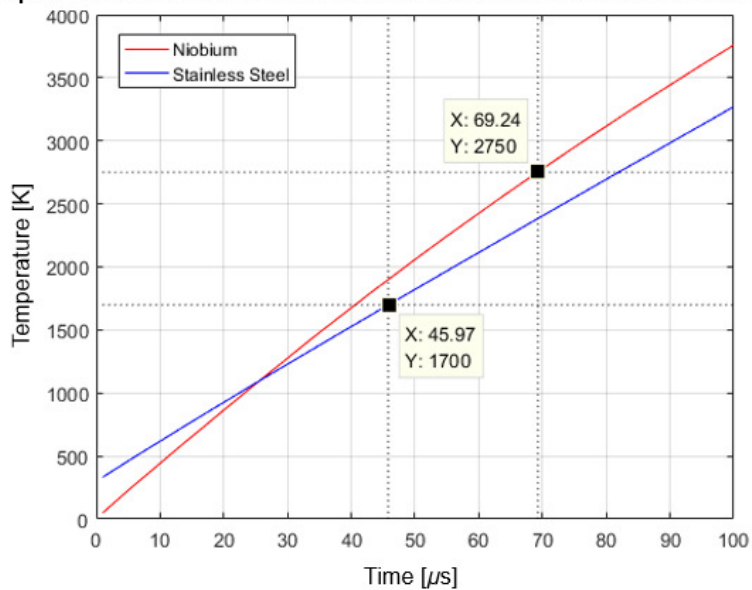
Figure 5. ANSYS thermal analysis of a uranium beam with 1 mm RMS radius and Gaussian profile, which is injected into Nb and SS with 90 degree grazing angle. The melting points of the two materials are 1673–1723°C (SUS304) and 2750°C (Nb). The times required to reach the melting points are ∼ 46 μs for SS and ∼ 69 μs for Nb.
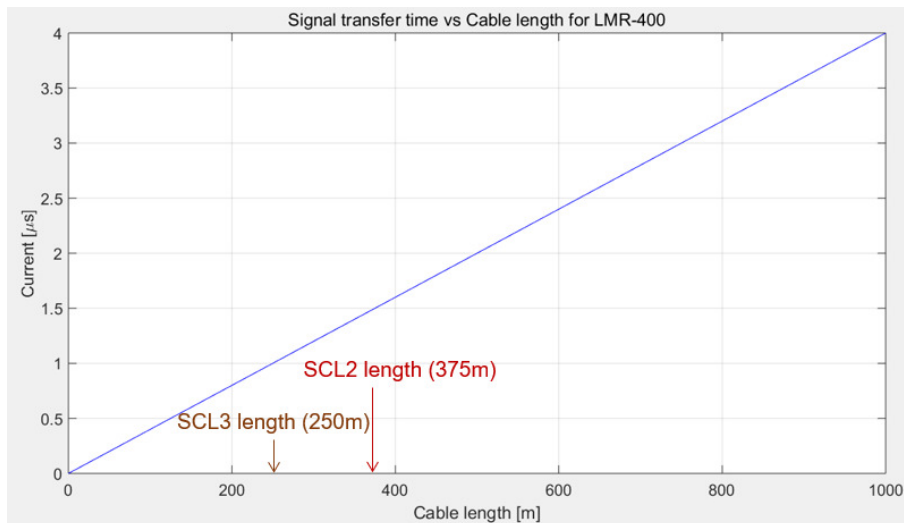

Figure 6. Signal transfer time as a function of cable length. The LMR-400 signal cable is expected to be used in the RAON BLM system.

3   MCNPX simulations of beam loss-induced radiation

3.1   MCNPX simulation settings

Before we design the optimal BLM configuration for the RAON, we must understand the characteristics of the beam loss-induced radiation. Charged particles, such as α or β particles, are not expected to penetrate through the beam pipe, but gamma and neutron radiation can be detected outside the beam pipe. We used the MCNPX (Version 2.7.0) Monte Carlo simulation tool to estimate the gamma and neutron radiation doses in the fast and slow loss cases.
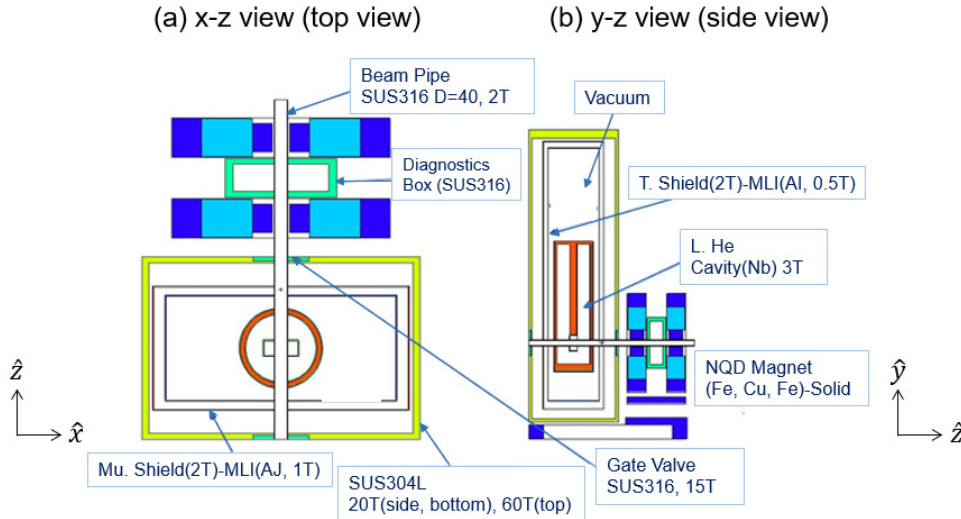

Figure 7. Structure of one of the quarter-wave resonator (QWR) units in the SCL31 section used in MCNPX simulation. (a) QWR geometry in the *x-z* plane. (b) QWR geometry in the *y-z* plane.

Figure 7 shows a geometric model of one of the quarter-wave resonator (QWR) units in the SCL31 section. All geometric models of the RAON accelerator facility are implemented in the simulation code including the sizes, material types, densities, and masses of major components [1, 3].

We performed simulations in both fast and slow loss situations using the MCNPX code. In the fast loss cases, we defined 1 W point sources of uranium (U), oxygen (O), and proton (H) beams with 10 mrad grazing angle, which strike one point of the inner surface of the beam pipe near the center of quadrupole magnet, as indicated by the red point in figure 8. It is assumed that the entire bunch of the beam would shift out of its original trajectory and head towards the surface of the beam pipe with 10 mrad grazing angle.

In the slow loss cases, we defined 1 W/m line sources of U, O, and H beams. The length of the line sources is set to be the length of the beam pipe (10 m), which spans over several warm sections. Each line source is assumed to produce a particle flux equivalent to 1 W/m. The line source is positioned at the center of the beam pipe, and emits particles randomly along all transverse directions. The grazing angle is set 90 degrees.

The simulations included two rectangular parallelepiped detectors right next to the beam diagnostic boxes to measure radiation. Figure 8 shows the simulation settings of the beam sources and detectors in the SCL32(1) section geometry with half-wave resonator 1 (HWR1) cavity. While
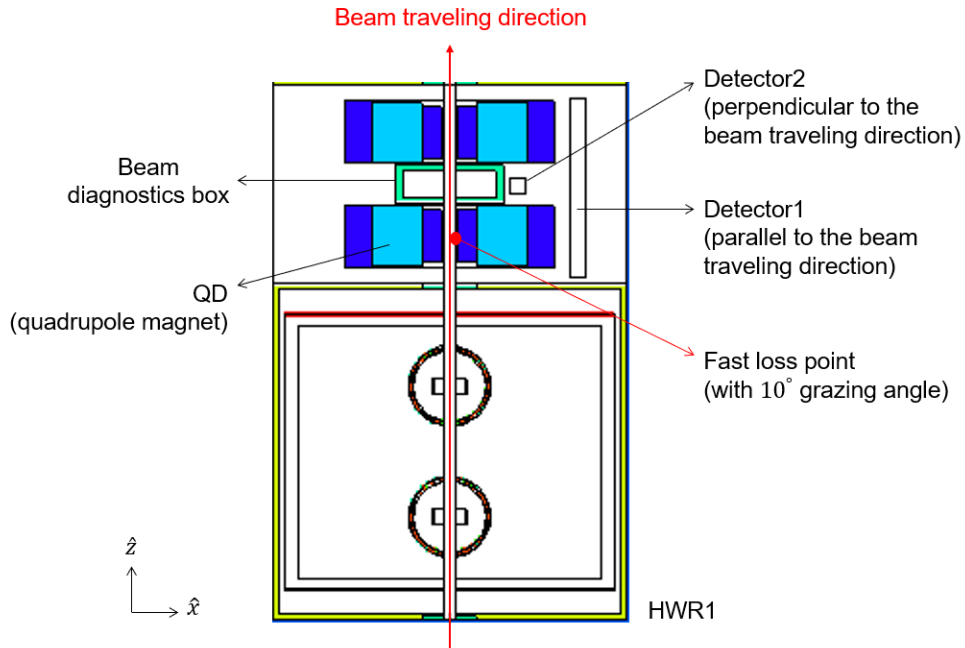
Figure 8. MCNPX simulation settings of the beam sources (fast loss: point source, slow loss: line source) and two detector options in the SCL32(1) section geometry with half-wave resonator 1 (HWR1) cavity. For the fast loss, a 1 W point source hits a point of the inner surface of the beam pipe with 10 mrad grazing angle near the center of quadrupole magnet (QD). Detector1 is positioned parallel to the beam propagation direction and detector2 is positioned perpendicular to the beam propagation direction.

detector1 is positioned parallel to the beam propagation direction, detector2 is positioned perpendicular to the beam propagation direction. Simulation settings for other sections of the linac are all the same other than the corresponding beam energy. The energy of the beam sources was defined differently while considering the beam energy in each acceleration section. Table 1 shows the energy variations of U, O, and H beams along the superconducting linac sections in RAON. The SCL31 is the lowest energy section and the energy increases as the beam enters the SCL22 section.

Table 1. Energy variations of uranium, oxygen, and proton beams along the superconducting linac sections in RAON. Energy is measured in MeV/u. The SCL31 is the lowest energy section and the energy increases as the beam enters the SCL22 section. The SCL21 and SCL22 sections are equipped with single spoke resonator (SSR) type cavities.

	SCL31	SCL32(1)	SCL32(2)	SCL21	SCL22
Cavity type	QWR	HWR1	HWR2	SSR1	SSR2
uranium	0.5 to 2.6	2.6 to 6	6 to 18.5	18 to 56.3	56.3 to 210.4
oxygen	0.5 to 4	4 to 10	10 to 34	34 to 90.8	90.8 to 325.7
proton	0.5 to 7.5	7.5 to 25	25 to 87.4	87.4 to 222	222 to 600

3.2 MCNPX simulation results
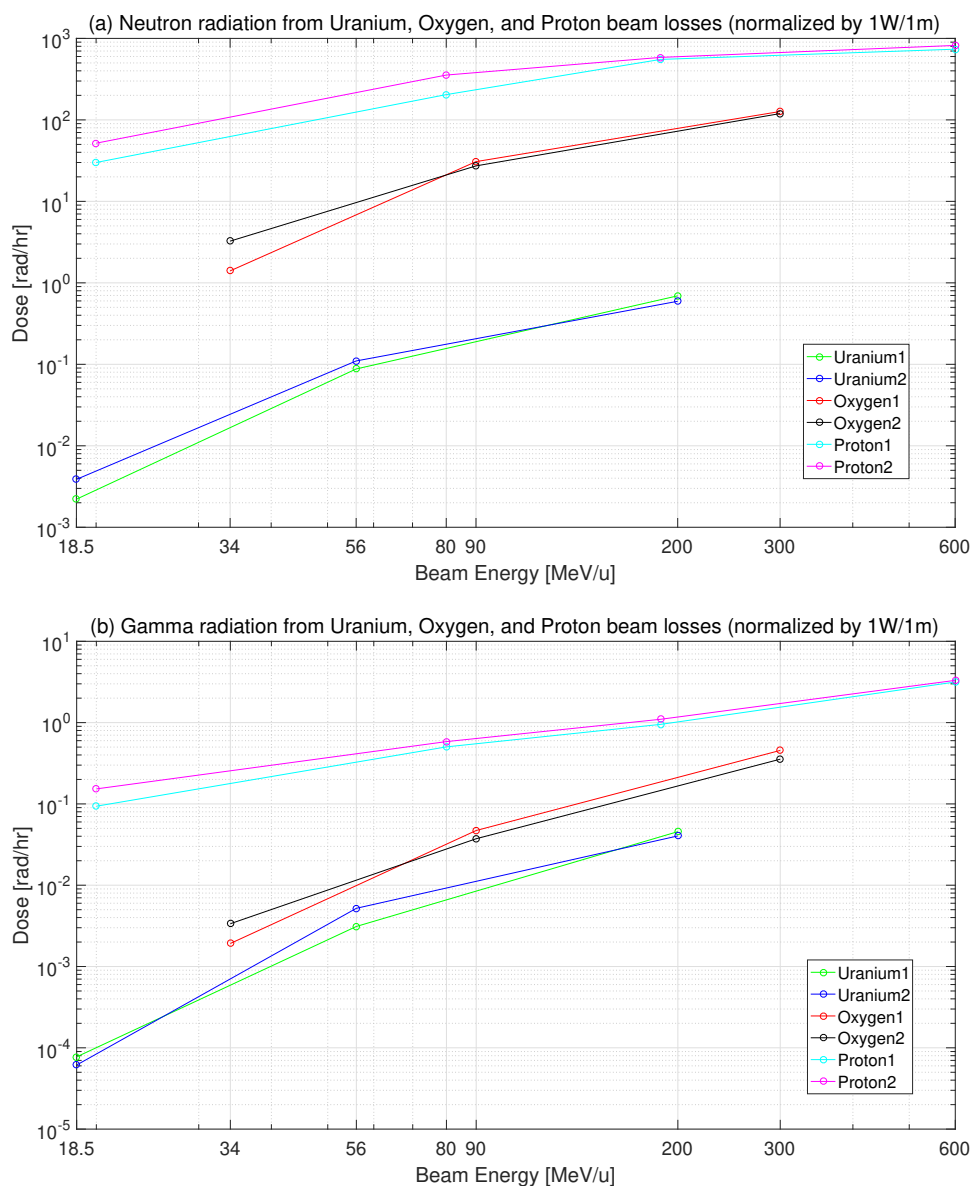
3.2.1 Radiation level

Figure 9. Normalized dose levels induced from 1 W/m slow losses of uranium, oxygen, and proton beams as functions of incident beam energy. The label 1(2) in the name of the beams indicates that detector1(2) is used to calculate the doses. (a) Neutron dose level (Normalized). (b) Gamma dose level (Normalized).

Using the simulation settings described in section 3.1, we first calculated the normalized neutron and gamma radiation levels in units of flux ($\#/cm^2/s$) and dose (rad/hr) for fast and slow losses with three different beams (U, O, and H). Figure 9 shows the normalized neutron and gamma dose levels associated with 1 W/m slow losses of U, O, and H beams. The label 1(2) in the name of the beam species indicates that detector1(2) described in section 3.1 was used to calculate the doses.

The normalized dose levels are used to calculate the expected current signal in the detectors we are interested in. Figure 9 shows that the overall radiation measurements at both positions are similar. The energy of each beam was chosen according to the table 1. As illustrated in figure 9, the detected radiation levels decrease for heavier beams with lower energy. For very low energies (< 10 MeV/u), the radiation levels are too low to be detected. Therefore, neutron or gamma detectors will not be used for these measurements, and destructive methods (e.g., beam loss collector made of niobium ring) are considered as alternatives. In particular, we note that monitoring beam loss of the uranium beam in the low energy linac section would be extremely challenging.

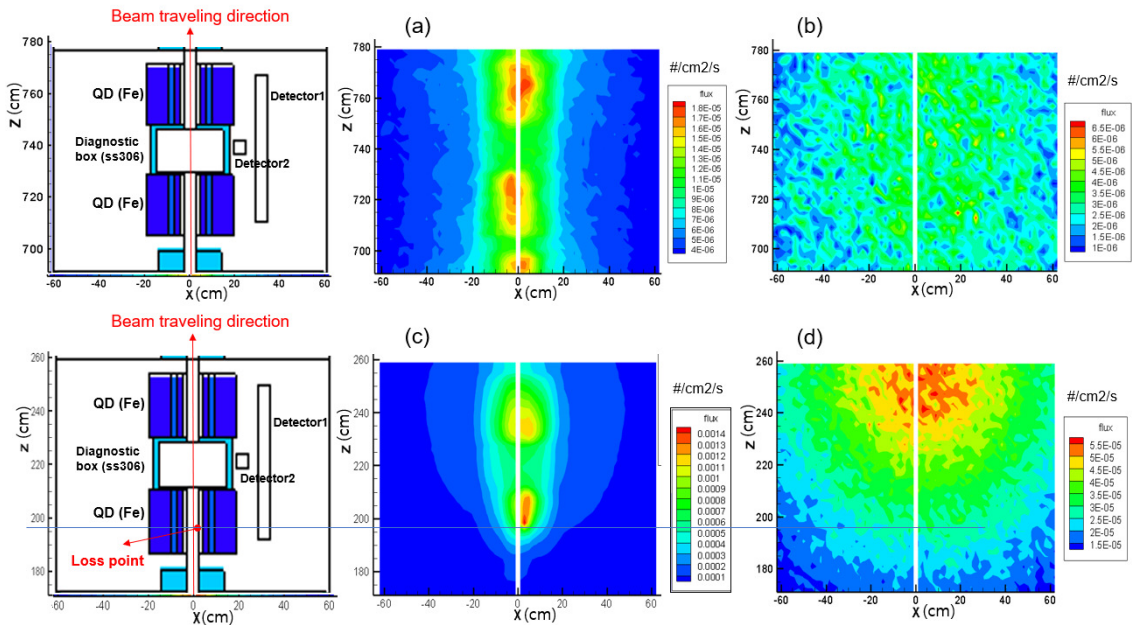### 3.2.2 Radiation dose map

Figure 10. Neutron and gamma dose maps outside the warm sections induced by losses from 200 MeV/u uranium beam. The radiation levels marked on these figures are in units of flux (#/cm^2/s). (a) Gamma dose map from 1 W/m line (slow) loss. (b) Neutron dose map from 1 W/m line (slow) loss. (c) Gamma dose map from 1 W point (fast) loss. (d) Neutron dose map from 1 W point (fast) loss.

Next, we draw dose maps that show the spatial distribution of radiation, which provide visual understanding of the radiation patterns. Figure 10 shows the neutron and gamma dose maps outside one of the warm sections of the SCL22 linac. Here, we assume that radiation is induced by losses from the 200 MeV/u uranium beam.

Figures 10 (a) and (b) show gamma and neutron radiation patterns, respectively, which originate from the 1 W/m line (slow) loss of the high-energy uranium beam. By contrast, figures 10 (c) and (d) show gamma and neutron patterns, respectively, from 1 W point (fast) loss of the uranium beam. The fast loss point is indicated with a red point near the center of the QD, which is indicated with the blue line in figure 10.

The gamma flux is not uniformly distributed around the QD because the elements of the QD are primarily constructed from Fe, which enhances interactions with gamma rays. Contrastingly,

the neutron flux has a rather uniform distribution because neutrons can penetrate materials with weaker interaction compared to gamma rays. In figure 10 (d), unlike the gamma flux distribution, the neutron flux is much higher near the end of the warm section than right next to the loss point. We note this arises because of the high penetration rate of neutrons.

Because of the lack of a complete list of beam loss scenarios, some strategy is required to determine the number of detectors and their locations [23]. TRACK beam dynamics simulations indicate that most localized losses occur in the quadrupoles, in which the beam size is largest [3]. Therefore, as a default, we plan to place one BLM per quadrupole doublet in the warm sections. Figure 10 implies that radiation fluxes are sufficiently localized such that one might tell at which doublet beam loss occurs. Fine-tuning of the BLM locations will be conducted during the commissioning phase of the RAON facility. We also note that the radiation dose patterns are more or less similar to beam losses in other sections of the linac and with different beam species, even though the absolute doses are different.

3.2.3 Radiation energy spectrum

Figure 11 shows the uranium beam loss-induced gamma (photon) and neutron energy spectrum. The overall radiation levels increase as the beam energy increases. Because gamma (photon) radiation is a high frequency EM field radiated in the processes of stabilizing the energy states of nucleus, they have limited energy ranges. By contrast, neutrons form through nuclear reactions (e.g., neutron evaporation) in such a way that they have broader energy ranges than gamma rays. We note that the y-axis values in figure 11 are given in arbitrary units, thus we can only gain relative information on the radiation energy spectra. Because gamma and neutron detectors have energy dependency, these energy spectra provide useful information in determining the proper BLM systems. Furthermore, the energy spectra of beam loss-induced radiation must be distinguished from the background radiation, which is not generated from beam loss itself. The background radiation issues will be discussed in the next section.

3.2.4 Background radiation

Strong photon radiation can arise not only from beam losses in the beam pipe but also from operation of the RF cavities. Bremsstrahlung radiation is generated from field-emitted electrons inside the cavities. These cavity X-rays indeed generate background noise in the BLM detectors, which can exceed the beam loss signal, particularly for heavy ions in the low energy sections [12, 20]. Therefore, we must separate background X-rays from beam loss-induced radiation when using BLM systems.

Figure 12 shows the background X-ray energy spectrum. Estimating the maximum X-ray dose in each linac section is summarized in table 2. In the simulation, the energy of the emitted electrons was set equal to the energy gained from the accelerating voltage in each cavity.

From figures 11 (a) and 12, we observe that the energy distribution of background X-rays lies at lower energy intervals compared with beam loss-induced radiation. Most X-ray energies are less than 1 MeV for low energy linacs. Therefore, we may use lead plates to shield low energy photons (<1 MeV) to reduce the effects of background cavity X-rays.
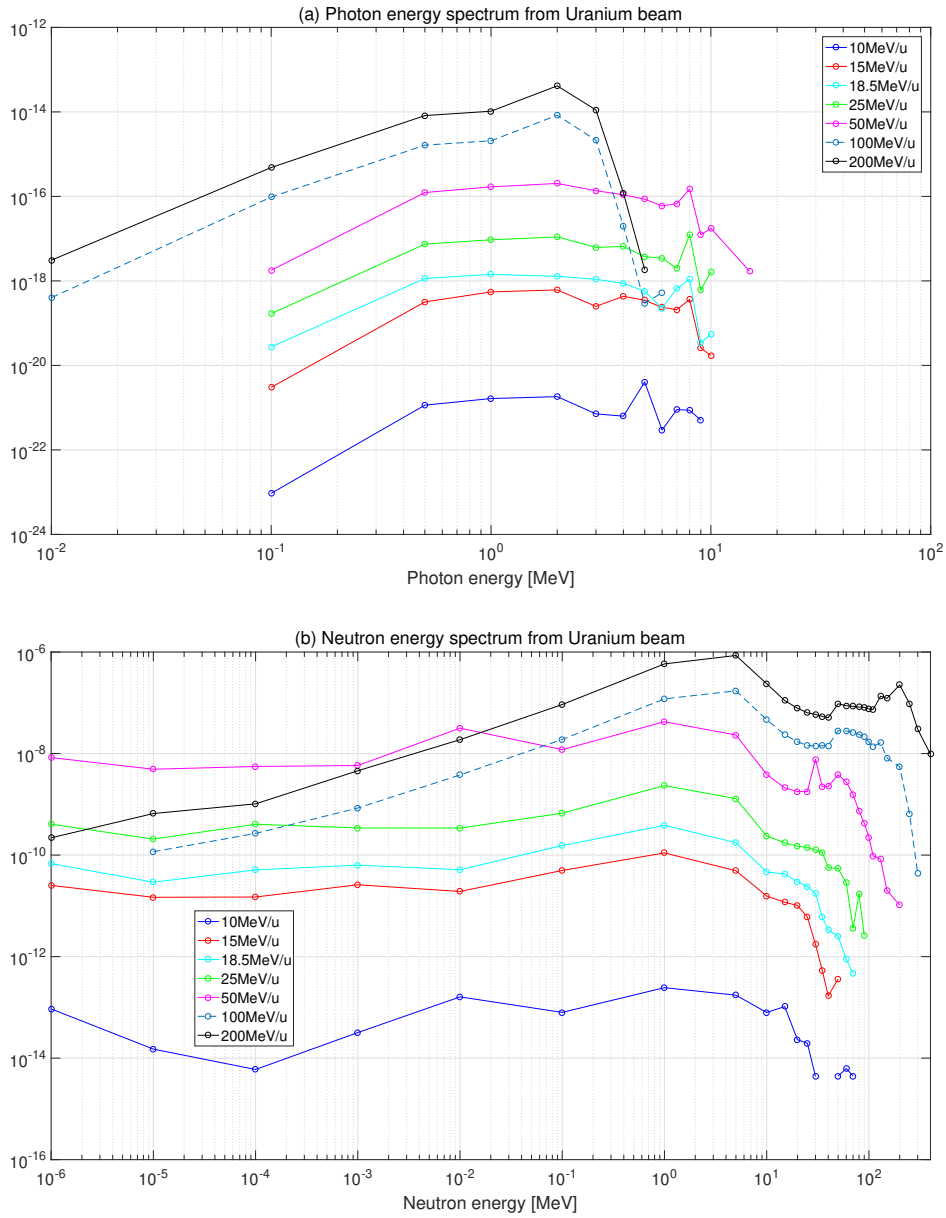
Figure 11. Energy spectrum of uranium beam loss-induced radiation. The overall radiation levels increase as the beam energy increases. (a) Gamma (photon) energy spectrum. (b) Neutron energy spectrum. The flux values on the *y*-axis are in arbitrary units.

4 Beam Loss Monitors (BLMs)

4.1 Types of beam loss monitors

Based on the simulation results presented so far (see section 3.2), we investigate the optimal BLM configuration for RAON. First, we consider plastic detectors (PDs) composed of plastic scintillators and photomultiplier tubes (PMTs). These detectors are fast and have high efficiencies for fast
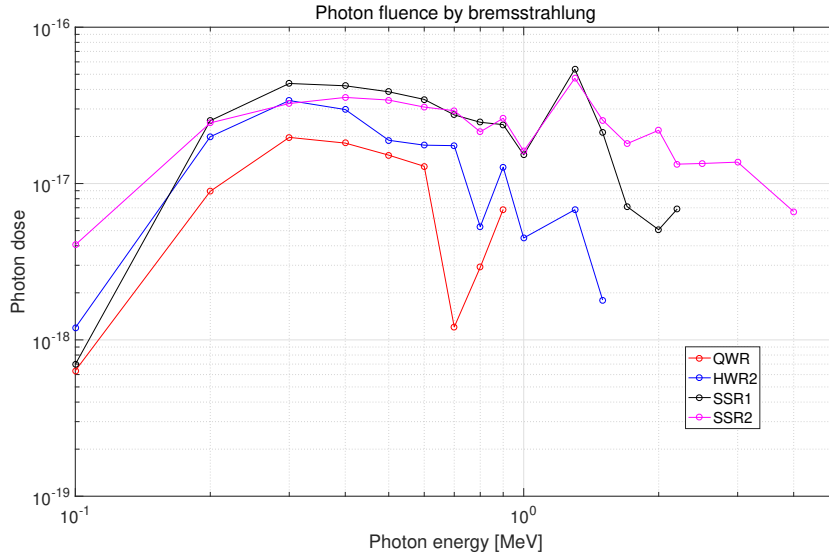
Figure 12. Background cavity X-ray energy spectrum. The energy of emitted electrons was set equal to the energy gained from the accelerating voltage in each cavity. The dose levels on the y-axis are in arbitrary units.

Table 2. Estimation of the maximum X-ray dose in each linac section.

	SCL11	SCL12(1)	SCL12(2)	SCL21	SCL22
Cavity type	QWR	HWR1	HWR2	SSR1	SSR2
Accelerating voltage (MV)	1.1	1.4	1.4	2.3	4.1
Maximum head load (W)	1.6	2.7	2.7	4.5	8
Maximum field emission flux (#/s)	9.1×10^{12}	1.2×10^{13}	1.2×10^{13}	1.2×10^{13}	1.2×10^{13}
Maximum dose (rad/hr)	3.75×10^{-2}	4.97×10^{-2}	4.97×10^{-2}	5.04×10^{-2}	5.03×10^{-2}

neutrons and high energy gamma rays [21]. BC-408 (or equivalently EJ-200) was used as a plastic scintillator material. This organic plastic is less sensitive to low energy X-rays and interacts with fast neutrons (> 50 keV) through (n,p) scattering. An R7724 PMT (2 in diameter, Hamamatsu) was used in the simulation. Considering the light output $R_s = 0.1$ photon/eV and the PMT gain is 7×10^5, the sensitivity (in Coulomb per rad) per 1000 g of BC-408 for photon is approximately [21]

$$S_{\text{scint}} \approx 118 \left[\frac{\text{C}}{\text{rad}} \right] \times \epsilon_{\text{coll}}, \tag{4.1}$$

where ϵ_{coll} is the efficiency of the collector or light guide, typically $50 \sim 70\%$. The detection efficiency (DE) of BC-408 to fast neutrons could be calculated based on the (n,p) scattering cross section. A 5 cm long BC-408 plastic scintillator was parameterized as follows [24]:

$$\text{DE}[\%] \approx -14.2 \ln(E_n) + 52.47, \tag{4.2}$$

where E_n is the neutron energy in MeV.

We also consider an ionization chamber (IC), which is included in nearly all accelerators. The sensitivity of an IC to a photon is [21]

$$S_{\text{IC}} \approx 100 \frac{\text{erg}}{\text{g}} \times \frac{1 \text{ eV}}{1.6 \times 10^{-12} \text{ erg}} \times \frac{1 e^-}{W \text{ eV}} \times \frac{\rho \text{ g}}{\text{cm}^3} \times V \text{ cm}^3 \times \frac{1.6 \times 10^{-19} \text{ C}}{1 e^-}, \tag{4.3}$$

where V is the volume of the chamber, ρ is the density of the gas injected into the chamber, and W is the W-factor (i.e., energy required to produce one electron-ion pair) of the gas. The calculated sensitivities for each gas in the IC are shown in table 3. Here, the volume of the chamber was considered to be 1 L.

Table 3. Calculated sensitivities of ionization chambers (IC) filled with 1 L of different gases.

Gas	Density (1 atm, 20°C) [g/cm^3]	W-factor [eV/e$^-$]	Sensitivity [nC/rad]
Ar	1.661×10^{-3}	26.4	638
N$_2$	1.165×10^{-3}	34.8	334
Air	1.204×10^{-3}	33.8	355.7

Because the sensitivity of the IC to the radiation dose resulting from proton or uranium beam losses is too low (only up to $\sim 600\,\text{nC/rad}$), we also consider the use of a proportional counter (PC), which has much higher sensitivity than an IC. The PC generates a larger number of ions and electrons inside the chamber, captures more electrons in the anode, and increases the intensity of the detected signal by applying a higher voltage than the IC. Figure 13 compares the current signals generated in the IC and PC according to the applied DC voltage. For example, the PC current would be a factor 10^3 larger than the IC current when the voltage is 2×10^3 V.
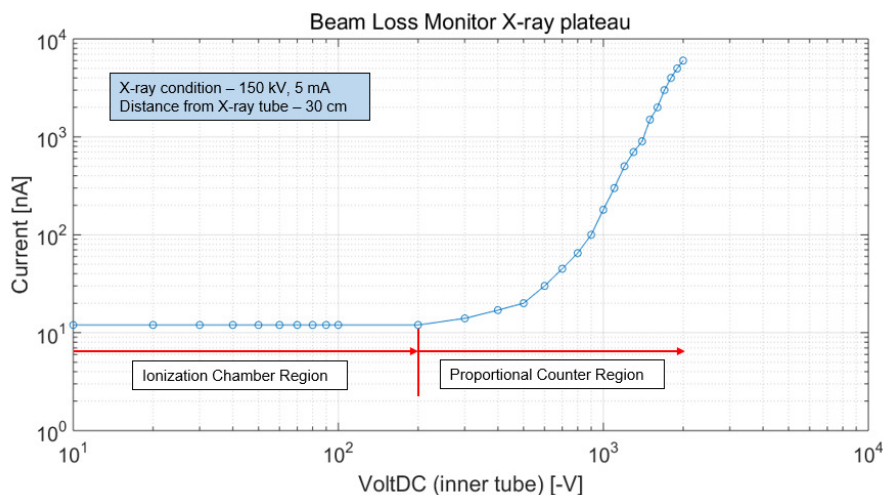

Figure 13. Comparison of the signal intensity in the PC and IC as a function of the applied DC voltage [25].

4.2 Expected signal in the beam loss monitors

Based on the MCNPX simulation results and the characteristics of the detectors, we calculated the expected current signal in the plastic detector (PD) for neutrons and the proportional counter (PC) for gammas (see figure 14). We assumed 1 W/m slow losses in both cases. As mentioned previously, the label 1(2) in the beam name indicates whether detector1(2) was used to calculate the radiation level. We note that detector 1 is positioned parallel to the beam propagation direction, whereas detector 2 is positioned perpendicular to the beam propagation direction.
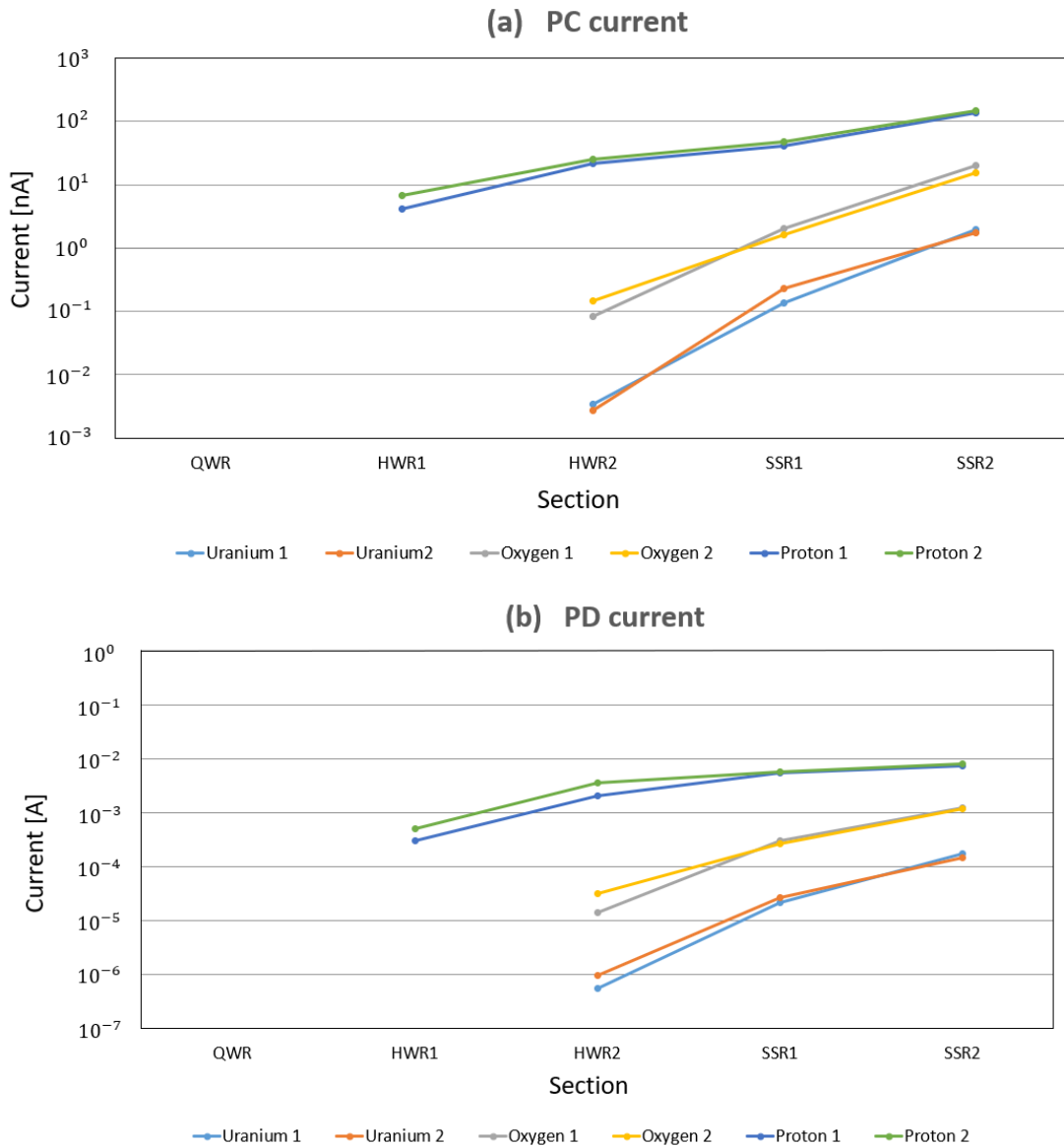
Figure 14. Expected current signal in the beam loss detectors calculated from the radiation levels in figure 9 for 1 W/m slow losses, and the sensitivities of the detectors introduced in section 4. The 1(2) label in the beam name refers to whether detector1(2) was used. (a) Proportional counter (PC) current signal for gamma detection. (b) Plastic detector (PD) current signal for neutron detection.

Regarding the PC current signal, we considered a mixture of Ar and CO_2 gases and a photon sensitive volume of $245\,cm^3$ (see figure 14 (a)). Regarding the PD current signal, we used the experimental calibration value of Korea Multi-purpose Accelerator Complex (KOMAC) [22], in which the sensitivity of BC-408 scintillator to neutrons is about $\sim 1\,mA/(Sv/h)$, and the detection volume is $\sim \pi(2.54/2)^2 \times 2.54\,cm^3$ (see figure 14 (b)). We assumed that lead bricks (50 mm thick) are used to shield against background cavity X-rays. A more detailed shielding strategy and background subtraction will be investigated during the initial beam commissioning phase.

5 Configuration of the RAON BLM system

The overall strategy of the detector types and locations in the RAON BLM system is summarized in table 4.

Table 4. Configuration of the RAON BLM system. DBCM: differential beam current monitor, BLC: beam loss collector, PD: plastic detector, PC: proportional counter.

Section	Cavity type	Primary BLM	Secondary BLM
SCL31	QWR	DBCM	BLC
SCL32(1)	HWR1	DBCM	BLC
SCL32(2)	HWR2	DBCM	BLC, PD
P2DT	—	DBCM	PD, PC
SCL21	SSR1	DBCM	PD, BLC
SCL22	SSR2	DBCM	PD, BLC

AC-coupled current transformers (ACCT's) are planned for installation before and after the sections where a beam transport monitoring is critical. The ACCT is a non-destructive beam current measurement device that uses the EM fields generated by a pulsed beam. When the current difference between ACCTs (transmission rate) deviates from the predicted value, an alarm signal for machine protection will be triggered. This differential beam current monitor (DBCM) network will be used as a primary MPS input for fast beam losses. The detector resolution is about $10\,\mu$A, and the rise time $(1$–$2\,\mu$s$)$ and signal conditioning are fast enough to accommodate an MPS interlock signal. For the DBCM, however, it is not suitable for 1 W/m slow loss detection owing to interference from RF noise.

In the case of a heavy ion accelerator, the secondary radiation for a given beam power loss is too low, and it is particularly difficult to detect them using the PC or PD in the low energy sections. Therefore, to increase the credibility of the BLM system, we consider the use of a beam loss collector (BLC) [12, 20], which is an interceptive device inside the beam pipe. It will be installed in every beam diagnostic box in the low energy sections, and in every 3 diagnostic boxes in the high energy sections (see figure 15). The BLC has very good sensitivity (a few tens nA for 1 W/m), is not susceptible to background X-rays, and is particularly effective in the low energy sections. Unlike the Faraday cup, there is no secondary electron suppressor in the BLC. Hence, the actual readout signal from the BLC can be as high as a factor ten larger than the intercepted currents depending on the secondary electron emission coefficient, which is a function of beam species and energy. One possible drawback for the BLC is the fact that the beam loss might damage the detector itself and contaminate the superconducting cavities.

One can infer from figure 14 (a) that the PC current signal would be too low for gamma detection, even in the high energy sections. Therefore, we decided to use PDs that are intended for neutrons detection in the high energy sections. From the end of the HWR sections, the PDs produce more than 100 nA for a 1 W/m uranium beam loss, which is larger than the assumed noise level [figure 14 (b)]. In the bending sections [post linac to driver linac transport (P2DT) and the charge stripper section (CSS)], the BLMs will be installed near the possible beam loss points, such as collimators and bending magnets. Because there are no RF cavities (i.e., no background X-ray noise) and there is a high probability of beam losses at these points, we can use PCs in the bending sections together with PDs. We note that PCs are more radiation-hard than PDs.
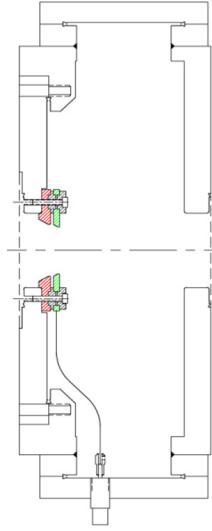
Figure 15. Layout of the beam diagnostic box with an installed beam loss collector. The pre-collimator (in red) is made of copper, and the ring-shaped collector (in green) is made of niobium. The beam travels from left to right.
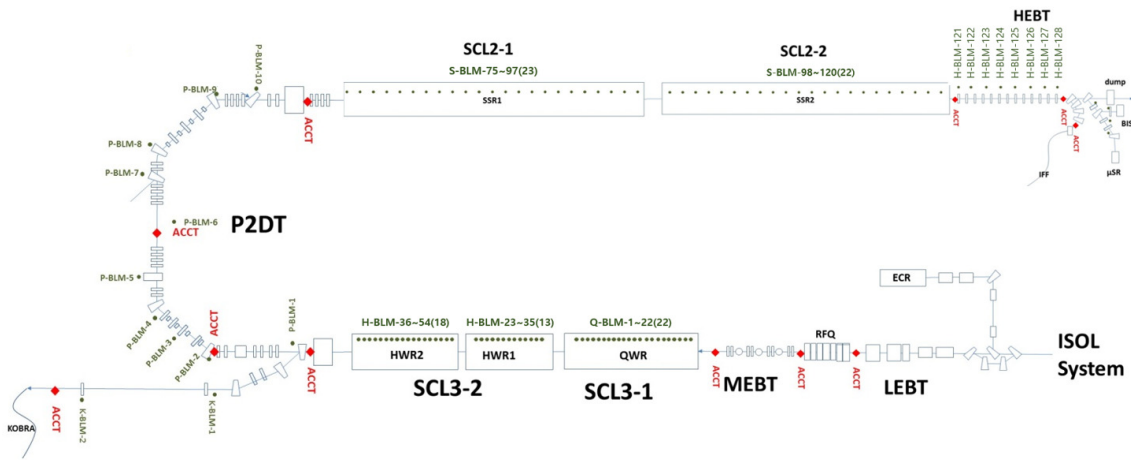
6 Conclusions

Figure 16. RAON BLM system layout. DBCM networks (pairs of ACCTs) are shown in red. Beam diagnostic chambers containing BLMs (BLC, PD, or PC) are shown in green.

Taking all these results and our discussion together, we arrive at the final layout of the RAON BLM system shown in figure 16. From the low energy sections (LEBT to SCL3) through the bending sections (P2DT, CSS) to the high energy sections (SCL2), we plan to install at least one BLM per warm section in the superconducting linac. In SCL3, the BLC will be installed at each beam diagnostic box, whereas it will be installed every 3 diagnostic boxes in SCL2 to produce a strong current signal for 1 W/m loss (> 100 nA). The ACCTs (DBCM network) are shown in red, which are placed at the start and end of the important acceleration structures.

From this design study of the RAON BLM system, we aim to establish a strategy for operating the high-power heavy ion (from proton to uranium beams) accelerator facility safely and efficiently. Beam loss situations and their locations can be detected reasonably quickly and accurately. The BLM system layout introduced in this study is still a work in progress, and it would be updated and improved during the beam commissioning phases and as the beam power increases. At present, PC and PD prototyping are underway, and test results with radiation sources will be reported elsewhere. Engineering design and fabrication of the diagnostics chamber with adapters for the BLC are also in progress.

Acknowledgments

References

[1] Rare Isotope Science Project (RISP) team, *RAON Accelerator and Experimental System Technical Design Report* (Volume 1, Project Overview), Institute for Basic Science (IBS), Korea (2013).

[2] T. Shin et al., *Rare Isotope Production and Experimental Systems of RAON*, *New Phys. Sae Mulli* **66** (2016) 1500.

[3] Rare Isotope Science Project (RISP) team, *RAON Accelerator and Experimental System Technical Design Report* (Volume 3, Accelerator Systems), Institute for Basic Science (IBS), Korea (2013).

[4] Rare Isotope Science Project (RISP) team, *RAON Accelerator and Experimental System Technical Design Report* (Volume 4, Experimental Systems), Institute for Basic Science (IBS), Korea (2013).

[5] Y.K. Kwon, *KoBRA for low energy nuclear physics study at RISP*, talk given at *KPS 2015 fall meeting*, Gyeongju, Korea, 2015 [https://nuclear.korea.ac.kr/indico/getFile.py/access?resId=5&materialId=slides&confId=141].

[6] Rare Isotope Science Project (RISP) team, *RAON Accelerator and Experimental System Technical Design Report* (Volume 2, Science), Institute for Basic Science (IBS), Korea (2013).

[7] J.M. Struckmeier and J. Klabunde, *On the stability and emittance growth of different particle phase space distributions in a long magnetic quadrupole channel*, *Part. Accel.* **15** (1984) 47.

[8] A. Pathak and S. Krishnagopal, *Higher order mode beams mitigate halos in high intensity proton linacs*, *Phys. Rev. Accel. Beams* **20** (2017) 014201.

[9] F. Gerigk, *Beam halo in high-intensity hadron accelerators caused by statistical gradient errors*, *Phys. Rev. ST Accel. Beams* **7** (2004) 064202.

[10] S. Lidia, *Diagnostics for high power accelerator machine protection systems*, in proceedings of the *3rd International Beam Instrumentation Conference*, Monterey, CA, U.S.A., 14–18 September 2014, pp. 239–249 [TUIYB1].

[11] C. Sibley, *Machine protection strategies for high power accelerators*, in proceedings of the *2003 Particle Accelerator Conference*, Portland, Oregon U.S.A., 12–16 May 2003, pp. 607–611.

[12] Z. Liu, T. Russo, R. Webber, Y. Yamazaki and Y. Zhang, *Beam loss monitor system for the low-energy heavy-ion FRIB accelerator*, in proceedings of the *2nd International Beam Instrumentation Conference*, Oxford, U.K., 16–19 September 2013, pp. 186–188 [MOPC46].

[13] P. Agrawal and W. Dally, *A hardware logic simulation system*, *IEEE Trans. Computer-Aided Design Integr. Circuits Syst.* **9** (1990) 19.

[14] M. Brugger, A. Ferrari, S. Roesler and L. Ulrici, *Validation of the FLUKA Monte Carlo code for predicting induced radioactivity at high-energy accelerators*, *Nucl. Instrum. Meth.* **A 562** (2006) 814.

[15] S.P. Yun, H.J. Kwon, J.H. Jang, K.T. Seol, H.S. Kim, B.S. Park et al., *Preliminary Operation of the Beam Loss Monitoring System at the 100-MeV Proton Linac*, in proceedings of the *4th International Particle Accelerator Conference*, Shanghai, China, 12–17 May 2013, pp. 601–603 [MOPME057].

[16] R.E. Shafer, *How Long a SNS Beam Pulse Would Damage a Copper Accelerating Structure?*, Spallation Neutron Source (SNS) Technical Note (2001).

[17] Y. Zhang, D. Stout and J. Wei, *Analysis of beam damage to FRIB driver linac*, in proceedings of the *15th International Conference on RF Superconductivity*, Chicago, IL, U.S.A., 25 July 2011, pp. 236–238 [MOPO058].

[18] H. Takei and H. Kobayashi, *Derivation of simple evaluation method for thermal shock damage on accelerator materials caused by out-of-control beam pulses and its application to j-PARC*, *J. Nucl. Sci. Technol.* **42** (2005) 1032.

[19] J.F. Ziegler, *SRIM: The Stopping and Range of Ions in Matter*, http://www.srim.org/.

[20] Z. Liu, F. Marti, S. Lidia, S. Cogan, M. Ikegami, T. Maruta et al., *Collimation design and beam loss detection at FRIB.*, in proceedings of the *57th ICFA Advanced Beam Dynamics Workshop on High-Intensity, High Brightness and High Power Hadron Beams*, Malmo, Sweden, 3–8 July 2016, pp. 400–403 [WEPM8X01].

[21] W. Wittenburg, *Beam Loss Monitors*, talk given at *CAS2008: Specialised Beeam diagnostics school*, Dourdan, France (2009), pp. 249–280.

[22] S-P. Yun et al., *Preliminary operation of the beam loss monitoring system at the 100-MeV proton linac*, in proceedings of the *4th International Particle Accelerator Conference*, Shanghai, China, 12–17 May 2013, pp. 601–603 [MOPME057].

[23] I. Dolenc Kittelmann and T. Shea, *Simulations and Detector Technologies for the Beam Loss Monitoring System at the ESS Linac*, in proceedings of the *57th ICFA Advanced Beam Dynamics Workshop on High-Intensity, High Brightness and High Power Hadron Beams*, Malmo, Sweden, 3–8 July 2016, pp. 553–558 [THAM6Y01].

[24] J. Va'vra et al., *Neutron Beam Line at SLAC*, SLAC-TN-14-026 (2014).

[25] Canon Electron Tubes and Devices, https://etd.canon/en/product/category/proportional/beamloss.html.